Eur. Phys. J. D **30**, 217–224 (2004)
DOI: 10.1140/epjd/e2004-00087-1

THE EUROPEAN PHYSICAL JOURNAL D

Surface second-harmonic generation in Au:TiO_2 cermet thin films

X. Quélin[1,a], M. Lemal[2], S.L. Gómez[3], and A. Bourdon[2]

[1] Laboratoire de Magnétisme et d'Optique de Versailles (UMR 8634), Université de Versailles, 45 avenue des États-Unis, 78035 Versailles Cedex, France
[2] Laboratoire des Milieux Désordonnés et Hétérogènes (UMR 7603), Université Paris-6, 140 rue de Lourmel, 75015 Paris, France
[3] Instituto de Fisica, Universidade de São Paulo, Caixa Postal 66318, São Paulo (SP), Brazil

Received 17 February 2003 / Received in final form 19 March 2004
Published online 6 July 2004 –

Abstract. The Surface Second-Harmonic Generation (SSHG) in Au:TiO_2 thin films of nanocermets is studied with samples of different metallic volume fractions using an IR Nd:YAG pulsed laser. We worked in a reflection geometry by varying the incidence angle and the directions of the incident beam polarization and of an analyzer of the Second Harmonic beam. We show that the SH signal is not due to electric dipolar processes only but can be treated within the general a, b, and d formalism where surfaces and bulk SH currents are well distinguished, and by describing the dielectric function of cermets within the effective-medium theory. The effective values obtained for a, b, and d are attributed to gold but the rather small discrepancies between them and those given by models are understandable by the fact that our samples are heterogeneous and not semi-infinite.

PACS. 42.65.Ky Frequency conversion; harmonic generation, including higher-order harmonic generation – 78.66.-w Optical properties of specific thin films – 78.30.Ly Disordered solids

1 Introduction

Electromagnetic properties in nanocermets which are composite materials made of metallic nanoparticles (typical diameter of 10 nm) embedded in a dielectric host, have been the subject of intensive theoretical [1,2] and experimental [3,4] researches in the last years. As shown by many studies, nanocermets have specific optical properties that are missing in metal and/or dielectric homogeneous media. For instance they exhibit giant enhancements in many nonlinear optical phenomena such as those seen in Raman scattering [5] and second harmonic generation (SHG) [4–6]. These enhancements have been associated to the optical excitation of surface plasmons (SP) which are collective electromagnetic modes that strongly depend on the structural characteristics of the composite medium.

At a low metallic concentration, metal nanoparticles are isolated from one another in the host. In this case, the SP resonance is peaked at a well-defined value depending on the dielectric properties of both the host and the metal but its spectrum exhibits only a slight dependence on the shape and the size of the nanoparticles [7]. When the metallic concentration (or filling factor) is increased, nanoparticles begin to aggregate forming clusters. At the percolation threshold corresponding to a phase transition between non-conducting and conducting (i.e. dielectric and metallic) states, a continuous electric path appears in the composite sample. In the vicinity of this percolation concentration, the sample structure exhibits a fractal geometry; consequently, surface-plasmon resonances are no more spectrally peaked but are excitable in all the visible and near-infrared range of the spectrum. Shalaev et al. [1,8] have proved that, for this fractal special geometry, SP tend to be localized on "hot spots". Above the metal-volume fraction at the percolation threshold, thin cermet films exhibit a metallic character for both optical [9] and electrical [10] properties.

The modes localized on "hot spots", at the origin of the electromagnetic enhancements, have been studied through linear and nonlinear optical phenomena with both 2D and 3D materials. In 2D films, also called semi-continuous metallic thin films, "hot spots", whose typical dimensions are much smaller than the incident half-wavelength, can be detected individually only with a near-field technique. In fact, they have been observed through optical near-field microscopy experiments [11,12]. "Hot spots" have been also recently observed in far-field using confocal microscopy [13], but in this case, the "hot spots" detected were the only ones to be strong enough ones for being coupled with propagating waves. On the contrary, in 3D-cermet samples, metallic particles are embedded in a dielectric host. The enhancement of electromagnetic fields in

[a] e-mail: quelin@physique.uvsq.fr

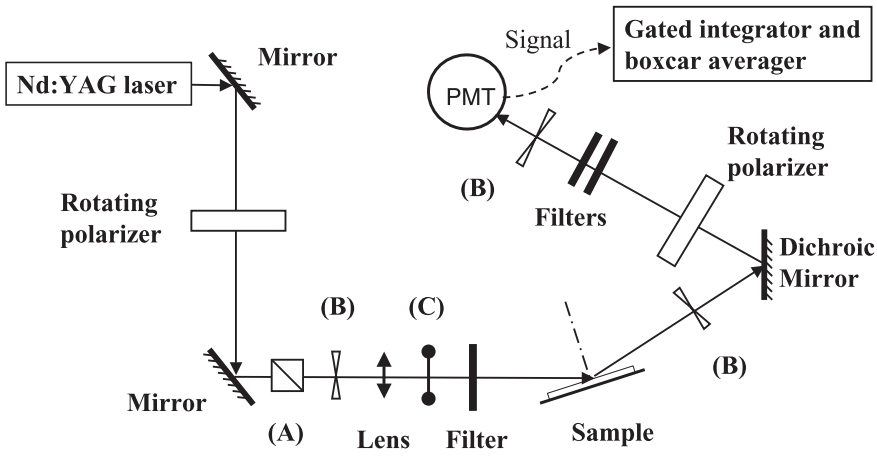

Fig. 1. Experimental set-up used for SH measurements in a reflection geometry. (A) denotes a Glan-Thomson polarizer used, together with the first rotating polarizer, for controlling the incident power. (B) denotes successive alignment pinholes and (C) corresponds to a half-wave plate for the incident wavelength ($\lambda = 1064\,\text{nm}$) used for rotating the incident beam linear polarization. The output SH beam is analyzed by a second rotating polarizer.

"hot spots" cannot be then directly observed, which makes near-field experiments with 3D samples not as relevant as those with 2D samples. Far-field techniques such as spectrophotometry [14], second harmonic generation [4], and Z-scan [15] are therefore still appropriate means for studying enhancements in 3D samples.

In this paper, we report a study on the optical surface-second-harmonic response of nanocermet thin films (gold particles embedded in a TiO_2 host) with different gold-inclusion characteristics (Sect. 2). The non-linear optical properties of cermets are explored with samples of metallic concentrations below and above the percolation threshold. The SH signal is studied by varying experimental geometrical parameters such as the angle of incidence and the directions of the linear polarization of the incident beam or of the output beam analyzer (Sect. 3). In Sections 4 and 5 is given first, an analysis of the experimental results where the SSH signals are proved not to be generated by electric dipolar processes only. No reliable model that takes other multipolar effects, into account, has been already published for surface-second harmonic generation (SSHG) in heterogeneous materials such as cermets. However as we want to compare our experimental results to those predicted by advanced appropriate SSHG models, we will content ourselves with checking models concerning homogeneous metal where non electric dipolar source terms are considered and take cermet as an effective homogeneous quasi-metallic medium. Finally, experimental results are found to be in good agreement with a slightly reinterpreted SSHG model where the inhomogeneous structure of nanocomposite samples is taken into account (Sect. 6).

2 Samples

Samples are prepared with the radio-frequency (RF) co-sputtering technique. A reactive gas (Ar and O_2) is introduced in the vacuum chamber to ensure titanium-dioxide stoichiometry. During the deposition, different parameters are strictly fixed to ensure the characteristics wished for the samples: work pressure is kept at $6.6 \times 10^{-3}\,\text{mbar}$; the float-glass-plate substrate is heated at 250 °C so as to stick the TiO_2 host material onto it; RF power is trimmed so as to obtain a low enough deposition rate of about 0.7 nm/mn. The gold concentration in the composite is controlled by displaying regularly a precise number of small gold disk-like pellets on the TiO_2 target. After deposition, the exact composition of the sample is determined by electron microprobe measurements and its thickness is measured with a profilometer. The calibration relation between the number of gold pellets and the sample composition is determined by measurements on layers of three different thicknesses. Sample thickness and crystallinity of the gold nanoparticles are also determined by X-ray-diffraction technique. We noticed that the Au diffraction-peak positions are only identical to the tabulated ones (JCPDS n° 04–0784) for the annealed samples (at 400 °C under atmospheric pressure during 24 h) [16]. Mean nanoparticle diameters (ϕ) are found to be between 5 and 10 nm; they are determined from the diffraction-peak widths through Scherrer's formula, $\phi = 0.9\lambda_X/\gamma\cos\theta_X$, where θ_X is the angle between the sample surface and the incident X-ray beam direction, λ_X the X-ray beam wavelength (Cu Kα_1) and γ the FWHM of the diffracted peaks [17].

Three samples are studied: samples (s1) and (s2) with gold-volume fractions (f) of 10% and 63%, respectively, and sample (s3) which is a 100% gold layer; their compositions are either below or above the percolation threshold close to 30% in the case of our 3D-nanocermets [18]. Sample thicknesses (e) are 79.8 nm, 133.2 nm, and 27.8 nm for (s1), (s2), and (s3) samples, respectively.

3 Experimental set-up

Surface-SHG experiments are performed with a Q-switched mode-locked Nd:YAG laser that provides 80-ps pulses in 200-ns packets at a repetition rate of 1 kHz. SHG measurements are carried out in a reflection geometry (Fig. 1). The incident IR beam ($\lambda = 1064\,\text{nm}$) is focused onto the sample surface and the energy of each pulse-packet is limited to $\sim$0.12 mJ to avoid any damage in the sample. The incidence angle (θ) with respect to the sample-surface normal and the polarization-direction (φ_1) of the linearly polarized incident beam can be both varied

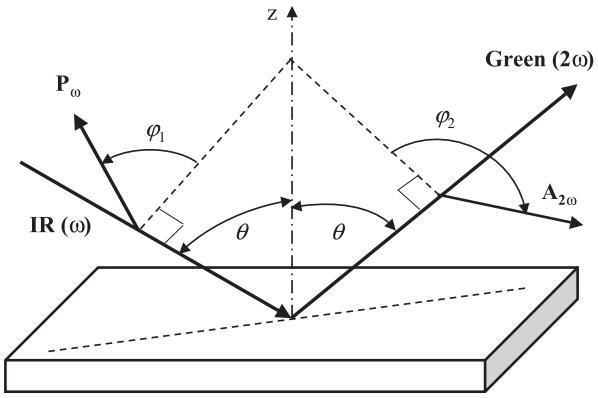

Fig. 2. Experiment geometry. The incidence angle is denoted θ while angles φ_1 and φ_2 give the direction of the linear polarization (P_ω) of the incident beam and that of the polarizer ($A_{2\omega}$) used to analyze the reflected SH beam, respectively ($\varphi_1 = 0\,^\circ$ corresponds to a p type incident polarization and $\varphi_1 = \pm 90\,^\circ$ to a s one).

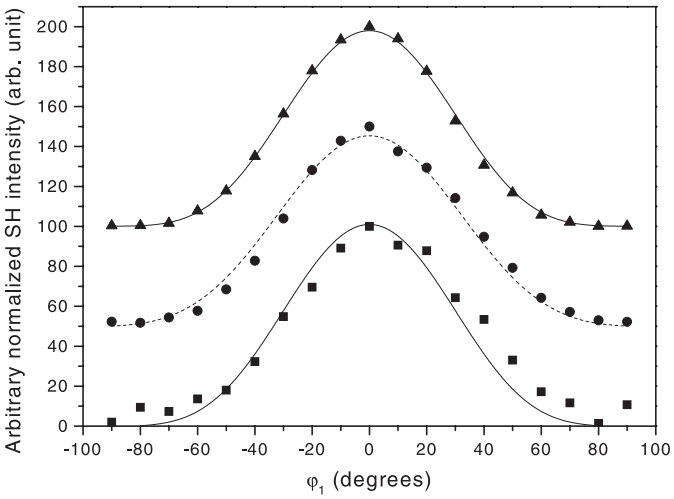

Fig. 3. Typical SH experimental intensity curves, (■), (•), and (▲) at a fixed angle of incidence ($\theta = 75\,^\circ$) and a fixed angle ($\varphi_2 = 0\,^\circ$ - p polarization), as functions of the incident polarization angle φ_1 with samples (s1), (s2), and (s3), respectively. Their corresponding well-fitting curves according to the a, b, d formalism are given too.

continuously by using a rotating polarizer (Glan-prism) and a rotating half-wave plate. As there is no reason for the SH electromagnetic field to be linearly polarized, it is linearly analyzed along a direction denoted (φ_2) by rotating another polarizer for a complete SSHG study (see Fig. 2). At least three different φ_2 values are necessary for the complete determination of an elliptical polarization state from intensity measurements. However this determination is less precise than the one made with specific ellipsometry technique. No prism is used for the incoming medium. As, in this configuration, the input medium is non-dispersive, the second harmonic beam propagates in the same direction as that of the reflected residual IR beam that has to be strongly rejected because the SH signal generated by nonlinear surface processes are very weak (the SSHG photon quantum efficiency being about 10^{-14} with our cermet samples). For that purpose, a dichroic mirror, several color filters, and an interference filter transmitting at 532 nm are used. The SH signal is then detected and measured by a fast and very linear photomultiplier tube whose photocathode-quantum efficiency is very low in the IR range (R928 Hamamatsu PMT). A gated integrator and a boxcar averager (SR250 Stanford Research Systems) are also used to improve the signal-to-noise ratio.

4 Experimental results

Our experimental results on surface SHG will be analyzed, in a first step, according to a surface electric dipolar model [19]. This first study needs, to be complete, to vary the three angular variables (θ, φ_1, and φ_2) independently (Fig. 2). The whole experimental data set is too large to be presented here, but three typical plots of the second harmonic intensity ($I_{2\omega}$) will be commented to make the three angular dependencies of $I_{2\omega}$ explicit.

Figure 3 shows a typical plot of $I_{2\omega}(\varphi_1)$ with the three samples; the incident polarization direction φ_1 is varied from $-90°$ to $+90°$ while the polarizer used to analyze the SH reflected beam is kept in a p configuration ($\varphi_2 = 0°$) and the incidence angle θ is fixed to 75°. Curves exhibit a nearly perfect symmetry with respect to the plane of incidence. The maximum of the signal is observed in the $[p-p]$ configuration (p directions for the ω and 2ω beams) whereas the $[s-p]$ configuration gives a much lower SH signal. The three curves also seem to follow the same $\cos^4(\varphi_1)$ law as the one observed with a continuous Ag film by Brown et al. [20], interpreted first by Jha [21,22], and cited by Bloembergen et al. [23]. The three curves shown in Figure 3 are arbitrarily normalized to 100 for $\varphi_1 = 0°$; they are (Oy) shifted to distinguish them and their respective best-fit curves according to equations given in Section 6, are shown on the same plot.

The $I_{2\omega}(\varphi_1)$ curves shown in Figure 4, are obtained at a fixed angle of incidence ($\theta = 30\,^\circ$) but with four different φ_2 values with the (s2) sample; $I_{2\omega}(\varphi_1)$ curves are no more even for $\varphi_2 \neq 0\,^\circ$ and $\varphi_2 \neq 90\,^\circ$.

Figure 5 is devoted to the study of the SHG signal in the $[p-p]$ configuration as a function of the incidence angle θ. Note our experimental θ range is wide enough to evidence the beginning of the decreasing part of the SH curve beyond the maximum already predicted by Jha [21,22].

Two remarks are obvious from these experimental data: (i) the SH field is much weaker in the output s polarization than in the p one and (ii) by varying the gold concentration in the samples, it is seen that the SH intensity is an increasing function of the gold concentration in the cermet (Fig. 5). A third complementary remark: (iii) as no signal is observed with pure TiO_2 thin samples, the optical SH process is proved to arises only from gold whatever its form, dispersed or continuous.

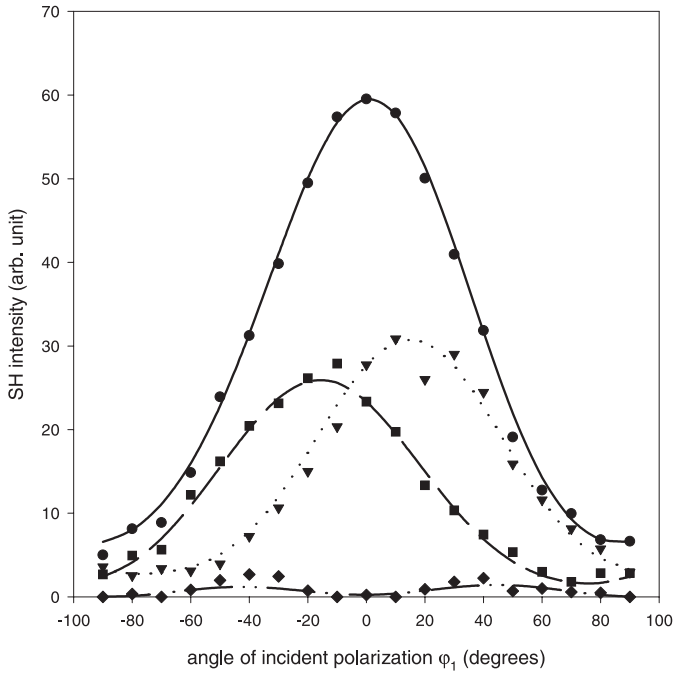

Fig. 4. Typical SH experimental intensity curves at a fixed angle of incidence ($\theta = 30^\circ$), as functions of the incident polarization angle φ_1, for four different output analyzer angles φ_2: (●) for $\varphi_2 = 0^\circ$ (p output polarization); (▲) for $\varphi_2 = -45^\circ$; (■) for $\varphi_2 = +45^\circ$ and (⧫) for $\varphi_2 = 0^\circ$ (s output polarization). It is clearly seen that the s output intensity is much weaker than the p one. To each experimental plot corresponds a best-fit curve obtained by our method detailed in reference [19].

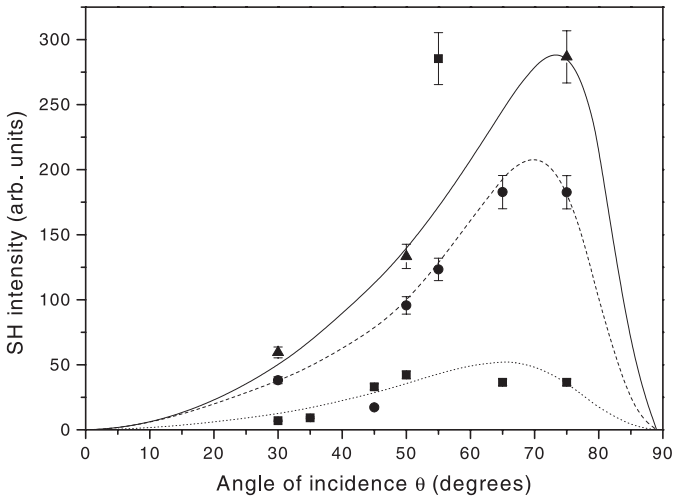

Fig. 5. SHG signal (■), (●), and (▲) in a $[p{-}p]$ configuration as a function of the incidence angle θ with samples (s1), (s2), and (s3), respectively. Corresponding well-fitting curves according to a, b, d formalism are given too. The experimental θ range is wide enough to evidence the beginning of the decreasing part of the SH curve beyond the maximum predicted by Jha. In this figure we have kept two absurd data points, but they have not be taken into account for the fitting procedure.

5 SHG data analysis according to a surface electric dipolar model

5.1 Method for a SH data analysis

We have recently presented a general method for the numerical determination, in the case of electric dipolar approximation, of the surface $\chi^{(2)}$ tensor from second-harmonic intensity measurements [19]. It is based on an experimental and theoretical system where a very thin nonlinear layer lies at the interface between two linear semi-infinite media and where no symmetry of the nonlinear surface is a priori assumed. Through a set of intensity measurements $I_{2\omega}$ (at least six different incidence angles θ, four different polarization directions φ_1, and three different angles φ_2, which implies at least 72 different measurements of $I_{2\omega}$) our method provides a complete determination of the 18 different complex elements of the $\chi^{(2)}$ tensor with the exception of only one overall arbitrary phase. It is a two-stage determination of $\chi^{(2)}$ that can be summarized as follows.

The first stage is a phenomenological SHG study at constant incidence angle θ. It is based on the fact that, in any "weak" SHG phenomenon, at constant incidence angle θ in a reflection geometry, the output field can be connected to the input field by an expression of the following type:

$$E_i^{(2\omega)} = M(\theta)_{ijk}\, E_j^{(\omega)}\, E_k^{(\omega)} \tag{1}$$

where i, j, and k are taken among the two input, s and p, polarization states. If $I_{2\omega}$ is measured from enough independent values of φ_1 and φ_2, a complex tensor $M^{\exp}(\theta)$ can easily be determined by a nonlinear best-fit procedure. There still remains one arbitrary phase per incidence angle on these intermediate data. No assumption is made about the origin of the SSH process in this stage.

In the second one, the $\chi^{(2)}_{lmn}$ complex values are found by a linear iterative procedure from the intermediate $M^{\exp}$ data as follows. As in the electric dipolar hypothesis, the connection between the phenomenological tensor M and $\chi^{(2)}$, the layer dipolar nonlinear characteristics, is linear and writes

$$M_{ijk}(\theta) = Q(\theta)_{ijk\ lmn}\, \chi^{(2)}_{lmn}, \tag{2}$$

where $Q(\theta)$ is an easily determined tensor that depends only on linear optical characteristics of the sample and on the geometrical parameters of the experiment; many reductions are also found when writing $Q(\theta)_{ijk\ lmn}$ in all the eight different equations (2), explicitly. An iterative determination of $\chi^{(2)}$ is then made from the set of $M^{\exp}(\theta)$ and $Q(\theta)$ tensors found at various incidence angles. Although the phase indetermination on each $M^{\exp}(\theta)$ is taken into account, only one overall phase indetermination on $\chi^{(2)}$ remains finally.

Table 1. Moduli (in arbitrary units) and phases (in rad) of $\chi^{(2)}_{ijk}$ obtained with the three samples (s1), (s2), and (s3), according to the method described in Section 5.

	sample (s1)		sample (s2)		sample (s3)	
ijk	$\|\chi^{(2)}_{ijk}\|$	$\arg(\chi^{(2)}_{ijk})$	$\|\chi^{(2)}_{ijk}\|$	$\arg(\chi^{(2)}_{ijk})$	$\|\chi^{(2)}_{ijk}\|$	$\arg(\chi^{(2)}_{ijk})$
xxx	15.6	−1.7	132.1	−1.5	93.1	−1.4
xyy	1.2	−2.8	6.9	−3.0	4.0	−2.5
xzz	184.7	−0.5	1501.1	−0.5	1121.1	−0.5
xyz	15.8	−2.0	107.5	−2.9	22.8	−2.9
xzx	93.6	2.0	764.4	2.2	532.7	2.3
xxy	2.1	0.7	15.7	−0.4	4.8	−0.5
yxx	2.4	2.7	2.0	0.07	5.8	2.8
yyy	0.1	−2.6	0.1	−1.1	0.3	−0.7
yzz	92.6	3.8	80.2	2.5	182.7	2.4
yyz	0.2	−2.3	0.5	1.0	0.5	0.95
yzx	16.3	0.07	14.4	−1.5	34.4	0.2
yxy	0.6	−2.8	1.7	0.5	1.6	0.4
zxx	48.6	2.5	397.8	2.7	280.1	2.7
zyy	11.8	1.9	17.7	1.5	17.1	2.5
zzz	90.9	0.5	734.6	0.5	574.0	0.5
zyz	152.1	2.2	904.7	1.2	131.3	1.5
zzx	318.4	0.0	2588.3	0.0	1933.2	0.0
zxy	21.0	−1.5	136.9	−2.5	26.06	−2.35

5.2 Analysis of experimental results with a surface electric dipolar approximation

The $\chi^{(2)}_{ijk}$ complex components we found for each sample with the above method, are given in Table 1 in the usual 3×6 matrix notation using a modulus/phase presentation. The arbitrary overall phase has been fixed by giving a zero phase to the $\chi^{(2)}_{zzx}$ component that has the largest modulus with all the three gold concentrations. No symmetry is seen in these data when compared to the three-rank tensor tables published for all the symmetry groups [24].

Nevertheless two kinds of very strong regularities are observed in the $\chi^{(2)}_{ijk}$ values found for different gold concentrations f in the cermet samples. In Figure 6, are shown plots of $(\|\chi^{(2)}_{ijk}(f=1)\|/\|\chi^{(2)}_{ijk}(f)\|)$ as functions of $\|\chi^{(2)}_{ijk}(f=1)\|$ for both concentrations 0.10 and 0.63. For a given f, this ratio is clearly constant for large values of $\|\chi^{(2)}_{ijk}\|$ whereas it is rather random for weaker ones. Similarly, it is clearly seen in Figure 7 that the phase of $\chi^{(2)}_{ijk}$ does not depend on f, for elements with large $\|\chi^{(2)}_{ijk}\|$. As the SH signal is proportional to the square of the SH field, it is mainly due to the largest $\chi^{(2)}_{ijk}$ components and then it can be roughly asserted that the three $\chi^{(2)}$ tensors exhibit a very similar structure although this structure corresponds to no point symmetry group (see Tab. 1). The $\chi^{(2)}$ tensors could eventually exhibit a very similar overall (independent of the orientation) asymmetric structure as the three samples differ only by their metal concentration. However as these samples were independently deposited on three different substrates and as the laser spot is randomly located, this eventual $\chi^{(2)}$ asymmetric structure should be randomly oriented in the xy-plane, which is not the case because the above ratio law is followed by the six largest $\chi^{(2)}_{ijk}$ elements. The above data analysis based on an electric dipole approximation leads then to a

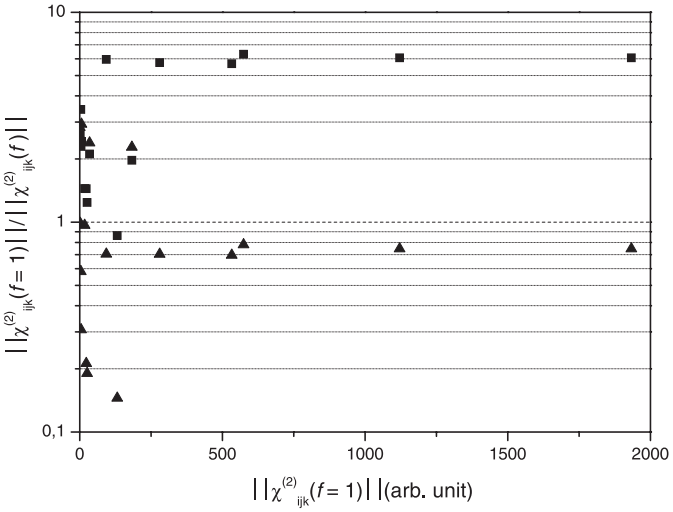

Fig. 6. Modulus of the ratios of the $\chi^{(2)}_{ijk}$ elements for a concentration $f=1$ and the $\chi^{(2)}_{ijk}(f=0.1)$ (■), and for the $\chi^{(2)}_{ijk}(f=0.63)$ (▲), as functions of $\|\chi^{(2)}_{ijk}\|$ for $f=1$ (the i, j, k indices are obviously the same for the χ_{ijk} elements to be compared). For large $\|\chi^{(2)}_{ijk}\|$, the ratios are evidenced to be constant for a given concentration.

Table 2. Values of the dielectric function at the fundamental $\omega = 1.17\,\text{eV}$ and at 2ω, for pure gold and titanium dioxide taken from reference [34]. In the following rows are given the effective dielectric functions calculated according to the Maxwell Garnett's theory and Bruggeman's one (2 solutions). In the right column is shown the penetration depth l_p, as defined in Section 6 for the three samples $\varepsilon(\omega)$ values, used to determine l_p, and $\varepsilon(2\omega)$ are taken from the same row.

		$\varepsilon(\omega = 1.17\,\text{eV})$	$\varepsilon(2\omega)$	$l_p(\omega)$ (μm)
Gold [34]		$-54.0 + i4.19$	$-6.29 + i2.04$	0.058
TiO_2 [34]		2.65	2.97	
Sample (s1) ($f = 0.1$)	Maxwell Garnett	$3.69 + i0.014$	$2.58 + i4.37$	
	Bruggeman sol. 1	$4.22 + i0.05$	$2.02 - i2.35$	0.535
	Bruggeman sol. 2	$16.93 - i1.51$	$2.69 + i1.51$	
Sample (s2) ($f = 0.63$)	Maxwell Garnett	$-27.11 + i2.33$	$-1.36 + i1.16$	
	Bruggeman sol. 1	$-20.37 + i1.92$	$-1.64 - i2.36$	0.086
	Bruggeman sol. 2	$-3.5 - i0.0058$	$-0.99 + i3.26$	

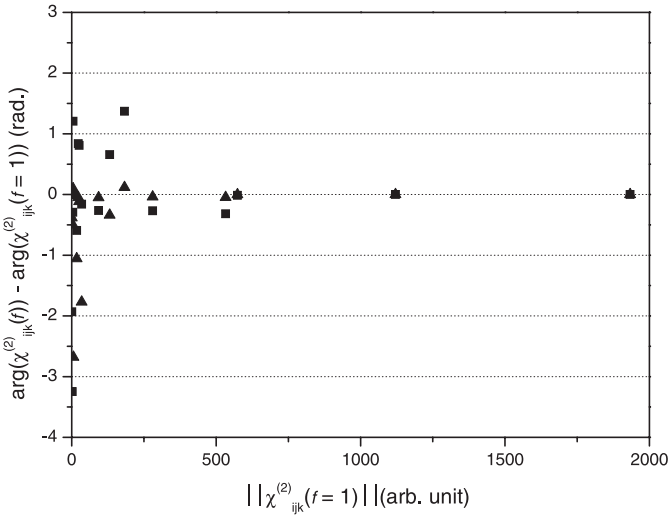

Fig. 7. Phase difference between $\chi^{(2)}_{ijk}(f = 0.1)$ and $\chi^{(2)}_{ijk}(f = 1)$ (■), and between $\chi^{(2)}_{ijk}(f = 0.63)$ and $\chi^{(2)}_{ijk}(f = 1)$ (▲), as functions of $\|\chi^{(2)}_{ijk}\|$ for $f = 1$ (the i, j, k indices are obviously the same for the χ_{ijk} elements to be compared). For large $\|\chi^{(2)}_{ijk}\|$, the $\chi^{(2)}_{ijk}$ phases are the same whatever the sample.

contradiction. If the SHG mechanism common to all samples cannot be due to an electric dipolar nonlinear polarization alone, the next terms in the multipolar expansion, such as magnetic dipolar and electric quadrupolar SHG, have to be taken into account too.

6 Comparison with models concerning homogeneous metal samples and discussion

Unfortunately we have no similar technique at our disposal to determine combinations of different higher order tensor components where no a priori symmetry is assumed. Another way is to compare our experimental results to those given by appropriate physical SSHG models but, unfortunately again, the only ones that take multipolar source terms into account, concern semi-infinite homogeneous metal samples. These models are based on various hypotheses: "extended plasma effects" [25], "hydrodynamic model" [26,27], "extended Thomas-Fermi-von Weizsäcker model" [28], and "local density approach" [29]. However in their analyses, the same parametric formulation is used to express the ratio $I_{2\omega}/I^2_\omega$ (see for instance Eqs. (2.1–2.4) of Ref. [29]) with three parameters $a(\omega)$, $b(\omega)$, and $d(\omega)$; this formulation is based on a clear separation between two surface currents, $j^{2\omega}_{//}$ parallel to the surface and $j^{2\omega}_{\perp}$ perpendicular to it, and a bulk one, corresponding to a, b, and d respectively.

Our experimental data will be described according to the same parametric formulation by determining, for each sample, the a, b and d parameters from experimental curves using a fitting procedure and comparing them to those given by theoretical models. The fitting procedure used according to equation (2.1) in reference [29], consists in checking sets of a, b, and d values that give simultaneously, for a sample, two curves that are very near experimental ones shown in Figures 3 and 5. Two preliminary observations can be made: (i) as our measurements are not absolute photometric ones, the ratio $I_{2\omega}/I^2_\omega$ we find, is known with one undetermined proportionality coefficient by sample. (ii) As the expression for $I_{2\omega}/I^2_\omega$ (Eq. (2.1) in Ref. [29]) is homogeneous with the three variables a, b and d, they can only be determined with the exception of the same complex proportionality coefficient and for their complete evaluations, an extra condition on a, b or d has to be found. The difference of nature between the two nonlinear media, cermet (the real one) and semi-infinite effective metal (theoretical), has to be analyzed before comparing our results with those given by models. Three aspects will be considered that will lead us to find some useful comparison tools: (i) for each sample the effective metal thickness (e) is far from being infinite and can be compared with the penetration depth (l_p), which yields the bulk coefficient d to be much lower than 1 which is the value given by all the models we considered above. We tentatively write

$$d = f\frac{\int_{-e}^{0}\exp\left(\frac{2z}{l_p}\right)dz}{\int_{-\infty}^{0}\exp\left(\frac{2z}{l_p}\right)dz} = f\left(1-\exp\left(\frac{-2e}{l_p}\right)\right), \qquad (3)$$

with $l_p = \lambda/\left(2\pi\sqrt{2\,\text{Im}\left(\varepsilon(\omega)\right)}\right)$ [30] (Tab. 2), λ being the fundamental wavelength. This assumption takes the

Table 3. Values of the parameters a_1, b_1, and d_1 as defined in Section 6, at the fundamental $\omega = 1.17\,\text{eV}$ and used in the fitting curves appearing in Figures 3 and 5. In the last three columns are given the parameters a, b, and d obtained by Liebsch and Schaich's (L.S.) and Chizmeshya and Zaremba's (C.Z.) models.

	sample (s1)	sample (s2)	sample (s3)	L.S. [29]		C.Z. [28]	
				TDLDA	LDA-RPA		
a_1	$-3.32 - i0.055$	$-3.19 - i0.12$	$-3.93 - i0.29$	$-17.2 - i4.0$	$-13.7 - i1.8$	-8.0	a
b_1	$-0.52 - i0.74$	$-0.16 + i0.15$	$-0.8 - i0.79$	-1	-1	-1	b
d_1	0.258	0.954	0.605	1	1	1	d

quadratic effects in SHG into account and, as $e \ll \lambda$, it is normal that no noticeable phase shift is brought to d. We will use this determination of d (see Tab. 3); it leaves a and b to be found without any proportionality coefficient from our experimental SSHG curves. (ii) Except for the (s3) sample, the metal cover is not totally spread over the sample surface. Let us define the following equivalent total-covering parameters, a_1, b_1, and d_1 by letting $a = fa_1$, $b = fb_1$, and $d_1 = 1 - \exp(-2e/l_p)$ [Eq. (3)]. Taking d_1 instead of d in the fitting procedure, a_1 and b_1 are then directly determined by taking advantage of the indetermination on the proportionality coefficient common to a, b and d. A second more subtle change due to the partial covering is the modification in the geometry of the current $j_{//}^{2\omega}$ parallel to the surface induced by frontal barriers yielding strong changes in the surface second harmonic polarization. On the contrary, as barriers induced by partial covering should not modify the $j_{\perp}^{2\omega}$ current, we will assume that the a_1 parameter should not be very far from that for a semi-infinite effective metal and could be compared to $a(\omega)$ values given by models. (iii) Roughness plays many roles: α- it makes the sample thickness e rather imprecise, β- it changes extra surface SH polarization, γ- the roughness finally brings, by its random structure, a well-known scattering effect. This item brings no quantitative information about a_1, b_1 and d_1 but it can be hoped roughness does not modify their values drastically when compared to those obtained with a smooth surface or flat sample. The random contribution in SH sources described above in the (ii) and (iii-γ) items generates SH diffuse scattering that decreases the specular reflection intensity. It is not the subject of this paper but has been recently studied with a nearly percolating cermet sample [31].

For the evaluation of a_1 and b_1 from equations (2.1–2.4) in references [29] and that of d_1 from equation (3), we need to previously know, at $\omega = 1.17\,\text{eV}$, the values of the dielectric functions $\varepsilon(\omega)$ and $\varepsilon(2\omega)$ for the three samples so as to determine the intermediate expressions for P, S, s, and l_p used in these equations. We have to determine the effective dielectric functions of the heterogeneous samples (s1) and (s2), and for that purpose, the two well-known effective-medium theories, Maxwell-Garnett's [32] and Bruggeman's [33], are used; $\varepsilon(\omega)$ and $\varepsilon(2\omega)$ are both needed for gold and titanium dioxide (see Tab. 2 [34]). Bruggeman's formula has two solutions (see Tab. 2); for $\varepsilon(\omega)$, one of them, very far from that given by Maxwell-Garnett's theory, is not used being considered as unrealistic while both solutions are taken for $\varepsilon(2\omega)$.

Some (a_1, b_1) pairs give well fitting curves (Figs. 3 and 5) but only one per sample, which will be the only one considered afterwards, gives for $\text{Re}(a_1)$ and $\text{Im}(a_1)$ values that lie in the $[-20, 0]$ range where the two models, those of Chizmeshya et al.'s (C.Z.) and Liebsch et al.'s (L.S.), that provide precise results (values or curves), locate their a parameter [28,29]. With the inhomogeneous samples, this good fitting (a_1, b_1) pair is found only by using Bruggeman's theory for $\varepsilon(\omega)$ and $\varepsilon(2\omega)$ and by taking the solution with $\text{Im}(\varepsilon(2\omega)) < 0$ (Tab. 2). We find for $\text{Re}(a_1)$ values that are very close to one another with the three samples; noticing sample (s3) is a pure gold film, it proves the gold origin of a_1. Our experimental a_1 values of about -3.50 can now be compared to the $a(\omega)$ values provided by C.Z. and L.S. models built for semi-infinite gold samples, at $\omega/\omega_p = \lambda_p/\lambda = 0.129$, where $\lambda_p = 138\,\text{nm}$ is the gold bulk plasmon resonance [35]. Both models depend on the atomic radius (r_s) of gold defined by $\left(4\pi r_s^3/3 = V_{el}\right)$ where V_{el} is the volume occupied by one conduction electron in the gold crystalline structure [36] ($r_s = 3.02$ atomic units). Checking C.Z.'s and L.S.'s results for this r_s value, gives: $a = -8.0$ (taking the 1/4 value for the "λ" parameter of the authors [28]), $a = -17.2 - i4.0$ (Time-Dependent Local Density Approach or TDLDA) and $a = -13.7 - i1.8$ (Local Density Approach-based Random Phase Approximation or LDA-RPA), respectively. The values we find for $\text{Re}(a_1)$ are about 44% the one obtained by C.Z., 20% the one obtained by L.S. in the case of TDLDA, and 26% the one for LDA-RPA, respectively (Tab. 3). As in models, the three a_1 complex values we find, have negative imaginary parts; they are particularly closed to the zero value obtained by C.Z. Our results for a_1 that are consistent with our assumption that SH surface currents perpendicular to the surface are not dephased by barriers, are closer to those found by C.Z. than to those given by L.S. The rather small discrepancy between model values and experimental ones could be interpreted as due to the roughness of our samples or to a stiffer surface-barrier height potential which tends to reduce the a value, as shown by L.S. [29].

The b_1 values characterizing the behavior of the SH parallel to the surface currents have been assumed above to be more modified by the cermet structure than a_1. In both models we considered, b is assumed to be (-1) whereas, for the three samples, we find for b_1 complex numbers whose real parts are all negative as with models and whose moduli are not too far from 1 (0.9 and 1.12

for samples (s1) and (s3), respectively), except for sample (s2) (we obtain 0.22 for this sample); no regularity is to be seen in their phases, and it is maybe due to the random aspects already mentioned about a_1 (Tab. 3).

7 Conclusion

Under powerful IR excitation, Au:TiO_2 cermets thin films clearly generate a weak but strong enough to be studied, Second Harmonic signal that is undoubtedly due to the gold component. A first analysis has shown that the Second Harmonic signal is not generated by electric dipolar processes. Following the a, b, and d formalism previously used by models that concern semi-infinite metallic medium and that take into account all the contributions to the total SHG signal, we have shown that this formalism can be also applied for our heterogeneous thin layers together with an effective medium theory for $\varepsilon(\omega)$. Moreover the values we obtain for the a, b and d parameters are not too far from those of pure semi-infinite gold treated by precise models, if we take into account that our samples exhibit many discrepancies from the semi-infinite model: roughness, small thickness, heterogeneity. Our experimental results show that it is conceivable to consider cermet thin films as an effective nonlinear medium that would have the same qualitative features of those of a metallic semi-infinite medium. We have seen that two Second Harmonic techniques provide complementary information about cermets: SH diffuse scattering is sensitive to the random structure of the microscopic inhomogeneities in cermets whereas our studies on SHG in a specular reflection geometry give smoothed characteristics of cermet samples.

Two authors (X.Q. and A.B.) wish to dedicate this work to the memory of M.L. One of the authors (S.L.G.) wish to thank Prof. P. Gadenne, the University of Versailles-Saint Quentin and COFECUB (Comité Français d'Évaluation de la Coopération Universitaire avec le Brésil) for their financial support.

References

1. V.M. Shalaev, A.K. Sarychev, Phys. Rev. B **57**, 13265 (1998)
2. A.K. Sarychev, V.A. Shubin, V.M. Shalaev, Physica B **279**, 87 (2000)
3. V.M. Shalaev, V.A. Markel, E.Y. Poliakov, R.L. Armstrong, V.P. Safonov, A.K. Sarychev, J. Nonl. Opt. Phys. Mat. **7**, 131 (1998)
4. R. Antoine, M. Pellarin, B. Palpant, M. Broyer, B. Prével, P. Galleto, P.F. Brevet, H.H. Girault, J. Appl. Phys. **84**, 4532 (1998)
5. *Surface Enhanced Raman Scattering*, edited by R.K. Chang, T.E. Furtak (Plenum, New York, 1982)
6. X. Quélin, J. Sakars, A. Bourdon, P. Gadenne, Physica B **279**, 102 (2000)
7. U. Kreibig, M. Vollmer, *Optical Properties of Metal Clusters* (Springer, Berlin, 1995)
8. A.K. Sarychev, V.A. Shubin, V.M. Shalaev, Phys. Rev. B **60**, 16389 (1999)
9. H. Raether, *Surface Plasmons on smooth and rough surfaces and on gratings* (Springer-Verlag, Berlin, 1988)
10. *Electrophysical Properties of Percolation Systems*, edited by A.N. Lagar'kov (Moscow, 1990)
11. S. Grésillon, L. Aigouy, A.C. Boccara, J.C. Rivoal, X. Quélin, C. Desmarest, P. Gadenne, V.A. Shubin, A.K. Sarychev, V.M. Shalaev, Phys. Rev. Lett. **82**, 4520 (1999)
12. P. Gadenne, X. Quélin, S. Ducourtieux, S. Grésillon, L. Aigouy, J.C. Rivoal, V.M. Shalaev, A.K. Sarychev, Physica B **279**, 52 (2000)
13. C. Anceau, S. Brasselet, P. Gadenne, J. Zyss, Opt. Lett. **28**, 713 (2003)
14. B. Palpant, B. Prével, J. Lermé, E. Cottancin, M. Pellarin, M. Treilleux, A Perez, J.L. Vialle, M. Broyer, Phys. Rev. B **57**, 1963 (1998)
15. N. Pinçon, B. Palpant, D. Prot, E. Charron, S. Debrus, Eur. Phys. J. D **19**, 395 (2002)
16. S. Liberman, X. Quélin, J. Sztern, Y. Dumont, A. Etcheberry, A. Bourdon, P. Gadenne, Eur. Phys. J. Appl. Phys. **11**, 91 (2000)
17. G.K. Williamson, W.H. Hall, Acta Meta. **1**, 22 (1953)
18. S. Berthier, *Optique des Milieux Composites* (Polytechnica, Paris, 1998), Chap. VII
19. X. Quélin, A. Bourdon, Opt. Comm. **208**, 197 (2002)
20. F. Brown, R.E. Parks, A.M. Sleeper, Phys. Rev. Lett. **14**, 1029 (1965)
21. S.S. Jha, Phys. Rev. Lett. **15**, 412 (1965)
22. S.S. Jha, Phys. Rev. A **140**, 2020 (1965)
23. N. Bloembergen, R.K. Chang, S.S. Jha, C.H. Lee, Phys. Rev. **174**, 813 (1968)
24. J.F. Nye, *Physical Properties of Crystals* (The Clarendon Press, Oxford, 1957)
25. J. Rudnick, E.A. Stern, Phys. Rev. B **4**, 4274 (1971)
26. C. Schwartz, W.L. Schaich, Phys. Rev. B **26**, 7008 (1982)
27. M. Corvi, W.L. Schaich, Phys. Rev. B **33**, 3688 (1986)
28. A. Chizmeshya, E. Zaremba, Phys. Rev. B **37**, 2805 (1988) (according to these authors, the most consistent results with those given by the Local Density Approach are found with $\lambda = 1/4$)
29. A. Liebsch, W.L. Schaich, Phys. Rev. B **40**, 5401 (1989)
30. M. Born, E. Wolf, *Principles of optics* (Cambridge University Press, Cambridge, 1980)
31. M. Breit, V.A. Podolskiy, S. Grésillon, G. von Plessen, J. Feldmann, J.C. Rivoal, P. Gadenne, A.K. Sarychev, V.M. Shalaev, Phys. Rev. B **64**, 125106 (2001)
32. J.C. Maxwell Garnett, Philos. Trans. R. Soc. Lond. **203**, 385 (1904)
33. D.A.G. Bruggeman, Ann. Phys. (Leipz.) **24**, 636 (1935)
34. E.D. Palik, *Handbook of Optical Constants of Solids* (Academic, New York, 1985), Vol. I, pp. 286-295 and pp. 795-804
35. N.W. Ashcroft, N.D. Mermin, *Solid State Physics* (Holt Saunders, New York, 1976)
36. *Handbook of Chemistry and Physics*, edited by D.R. Lide 75th edn. (CRC Press, Boca Raton, 1995), pp. 4-139